

# Nanostructured Photocatalytic TiO<sub>2</sub> Coating Deposited by Suspension Plasma Spraying with Different Injection Positions

Xuezhong Liu<sup>1,2,3</sup> · Kui Wen<sup>2,3</sup> · Chunming Deng<sup>2</sup> · Kun Yang<sup>2</sup> · Changguang Deng<sup>2</sup> · Min Liu<sup>2</sup> · Kesong Zhou<sup>2,3</sup>

Submitted: 21 August 2017 / in revised form: 3 January 2018 / Published online: 26 January 2018  
© ASM International 2018

**Abstract** High plasma power is beneficial for the deposition efficiency and adhesive strength of suspension-sprayed photocatalytic TiO<sub>2</sub> coatings, but it confronts two challenges: one is the reduced activity due to the critical phase transformation of anatase into rutile, and the other is fragmented droplets which cannot be easily injected into the plasma core. Here, TiO<sub>2</sub> coatings were deposited at high plasma power and the position of suspension injection was varied with the guidance of numerical simulation. The simulation was based on a realistic three-dimensional time-dependent numerical model that included the inside and outside of torch regions. Scanning electron microscopy was performed to study the microstructure of the TiO<sub>2</sub> coatings, whereas x-ray diffraction was adopted to analyze phase composition. Meanwhile, photocatalytic activities of the manufactured TiO<sub>2</sub> coatings were evaluated by the degradation of an aqueous solution of methylene blue dye. Fragmented droplets were uniformly injected into the plasma jet, and the solidification pathway of melting particles was modified by varying the position of suspension

injection. A nanostructured TiO<sub>2</sub> coating with 93.9% anatase content was obtained at high plasma power (48.1 kW), and the adhesive coating bonding to stainless steel exhibited the desired photocatalytic activity.

**Keywords** numerical simulation · photocatalytic coatings · suspension plasma spraying · TiO<sub>2</sub> coating

## Introduction

Titanium dioxide (TiO<sub>2</sub>) is a semiconducting material sensitive to photons, which has potential applications in solar energy conversion, gas sensors, and organic degradation of polluted air and wastewater (Ref 1-3). The properties of photocatalytic TiO<sub>2</sub> are strongly correlated with phase composition, crystal size and specific surface area. Due to quantum effects of nanometer crystallites and augmented surface area, nanostructured TiO<sub>2</sub> is an optimal choice as the photocatalyst. Anatase and rutile are two important phases of titanium dioxide, which have outstanding stability and photoactivity. Recently, some researchers reported that a mixed crystal of anatase and a certain amount of rutile phase exhibited better photocatalytic performance than that of neat anatase (Ref 4, 5). However, TiO<sub>2</sub> nanoparticles with high content of anatase phase are still deemed to present high photocatalytic activity.

Suspension plasma spraying (SPS) is a novel method to deposit nanostructured coatings. It can inject a liquid suspension of submicron powders or nanoparticles into a plasma jet rather than agglomerated micro-powders. Much interest has been expressed to immobilize TiO<sub>2</sub> particles in coatings by this method (Ref 6, 7).

✉ Xuezhong Liu  
Xuezhong\_liu@126.com

Kesong Zhou  
kszhou2004@163.com

- <sup>1</sup> School of Materials and Mechanical Engineering, Jiangxi Science and Technology Normal University, Nanchang 330013, People's Republic of China
- <sup>2</sup> National Engineering Laboratory for Modern Materials Surface Engineering Technology, The Key Lab of Guangdong for Modern Surface Engineering Technology, Guangdong Institute of New Materials, Guangzhou 510651, People's Republic of China
- <sup>3</sup> School of Materials Science and Engineering, Central South University, Changsha 410083, People's Republic of China

By dispersing TiO<sub>2</sub> nanoparticles in deionized water, Toma et al. (Ref 6) deposited dense coatings by SPS, and degradation of air pollutants was achieved by the coating with an anatase phase content higher than 16 vol.%. Later, TiO<sub>2</sub> coatings with high porosity were deposited by plasma spraying of aqueous titanium isopropoxide. However, with the increase of plasma power, the anatase content decreased (Ref 4). In addition, the stand-off distance imposed great effects on the phase composition and microstructure, and the anatase content increased with the increasing of the stand-off distance (Ref 8). Kozerski et al. (Ref 5) compared TiO<sub>2</sub> coatings deposited by using different injectors. The anatase content in the coatings deposited by the internal continuous-stream injector varied from 1.6 to 8.8 vol.%. However, the anatase content using an external atomizing injector varied in the range of 9.4–15.4 vol.%.

Moreover, Daram et al. (Ref 9) prepared a titanium dioxide/carbon nanotubes composite coating, which presented a higher photocatalytic performance than a TiO<sub>2</sub> coating containing the rutile phase. In the view of thermodynamics, the anatase phase presents low Gibbs free energy and is more stable than the rutile phase when the granular size is below 15 nm. Thus, Robinson et al. (Ref 10) utilized dilute suspensions of TiO<sub>2</sub> nanoparticles (average size > 12 nm) synthesized by hydrothermal flow as a feedstock. After suspension plasma spraying, nanostructured TiO<sub>2</sub> coatings predominantly containing the anatase phase were obtained.

Briefly, the challenge of depositing photocatalytic TiO<sub>2</sub> coatings with suspension plasma spraying is the achieving of adherent coatings with plenty of anatase phase (Ref 11). Low plasma power is favored to deposit nanostructured TiO<sub>2</sub> coatings with high content during suspension plasma spraying, but the deposition efficiency and cohesive strength of TiO<sub>2</sub> coatings are generally poor. High plasma power is beneficial for the deposition efficiency and cohesive strength of TiO<sub>2</sub> coatings, but it produces two challenges: the decreased coating activity due to critical transformation of anatase into rutile, and the fragmented droplets of the suspension cannot be injected into the plasma core. It seems difficult to deal with the dilemma by spray parameters alone.

In this paper, TiO<sub>2</sub> coatings deposited by SPS with different injection positions were studied under the guidance of numerical simulation, which was derived from a realistic three-dimensional (3D) time-dependent numerical model that included the inside and outside of the torch regions. Moreover, detailed research about the microstructure, phase composition, and photocatalytic performance of TiO<sub>2</sub> coatings was conducted.

## Experimental

### Materials

Coatings were sprayed from a stable TiO<sub>2</sub> suspension with particle size about 30 nm (anatase > 99 wt.%). Distilled water was used as a solvent, and solid loading in the suspension was fixed at 15 wt.%. Stainless steel disks ( $\Phi 30 \times 5$  mm) were used as substrates. Prior to coating deposition, the substrates were polished with a fine grade of sandpaper and consequently cleaned with ethanol to remove contaminants.

### Suspension Plasma Spraying

Suspensions plasma spraying were carried out using an F6 torch (GTV Verschleißschutz) with a 6-mm internal diameter anode. The flow rate of Ar gas was set as 40 slpm, whereas the flow rate of hydrogen was 10 slpm. Though the position of the suspension injection was addressed according to simulation results, the distance between the substrate and the outlet of the plasma gun was fixed at 90 mm throughout the experiments. The TiO<sub>2</sub> suspension was radially injected into the plasma jet through a nozzle with average diameter 0.3 mm by a suspension feeder (GTV Verschleißschutz). For all coatings, the feed rate of the suspension was fixed at 30 ml min<sup>-1</sup>.

### Coating Characterization

Scanning electron microscopy (FE-SEM; Nova-Nona-430; FEI) was conducted to investigate the morphology and microstructure. X-ray diffraction (XRD; Smartlab 9 kW; Rigaku) was adopted to analyze the phase composition. Raman spectroscopy (LabRAM HR800; HORIBA Jobin-Yvon) and UV-Vis spectroscopy (HP8453; Keysight) were used to characterize the coatings.

### Photocatalytic Activity

Photocatalytic activity was evaluated by decomposing a 5-ppm methylene blue (MB) solution. Samples were immersed in the MB solution (50 ml), then placed in a home-made set-up and irradiated using a UV-lamp. The wavelength was 370 nm and the intensity was 2.5 mW/cm<sup>2</sup>. A 6-ml volume of MB solution was withdrawn after a certain period of irradiation, and the absorbance was measured to determine the MB concentration using a spectrometer. The measurement wavelength was set at 664 nm, referencing the distinctness of the absorption peak of MB. Meanwhile, a blank sample without a TiO<sub>2</sub> coating was also tested.

## Results and Discussion

### Injection Positions

The plasma jet without a suspension injection was first measured by the Enthalpy Probe System (Tekna Plasma Systems, Canada) at a stand-off distance of 90 mm. The results of the plasma temperature and velocity with different arc currents are shown in Fig. 1. The temperature was obtained by calculating the energy balance of the circulating cooling water in the enthalpy probe, while the plasma velocity (low Mach number of gas flow) was directly calculated by the Bernoulli equation. As seen in Fig. 1, the plasma temperature increases from 2730 to 2880 K with the arc current raising from 450 to 650 A (the corresponded plasma power increases from 32.4 to 48.1 kW). As some publications have reported (Ref 8, 11), it was difficult to avoid the metastable anatase phase converting to rutile under the condition of high plasma power. In fact, the transformation temperature of anatase TiO<sub>2</sub> to rutile is about 400-900 K. Once it was deposited onto the substrate, the transformation of sprayed TiO<sub>2</sub> anatase to rutile can be induced subsequently by heating of a sequential scan of the plasma jet (Ref 12).

Because the measurement distance by the Enthalpy Probe System to the nozzle exit must be longer than 60 mm to avoid thermal overload, it cannot directly diagnose the plasma jet at the exact locality of the suspension injection. Thus, a realistic 3D LTE (Local Thermal Equilibrium) numerical model without suspension injection, where the computational domain included the inside and outside regions of the torch, was developed to investigate the plasma jet (Ref 13-15). We found that there is a coexistence of multiple arc roots. The particular plasma arc attachment location leads to a significant asymmetry in the distributions of temperature and velocity as well as the

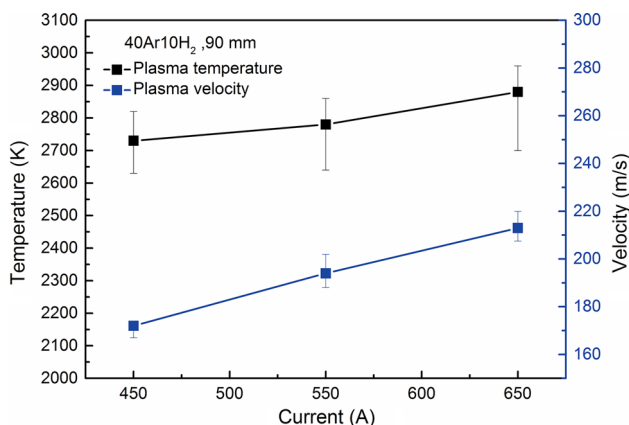


**Fig. 1** Plasma temperature and velocity with different arc currents measured by the Enthalpy Probe System at a stand-off distance of 90 mm (Ar/H<sub>2</sub>: 40.0/10.0 slpm)

electric potential and field strength. The continuous movement of the plasma arc not only causes fluctuation in the arc voltage drop but also results in temporal variations of the plasma temperature and velocity. Figure 2(a) and (b) illustrates the typical simulation results, which corresponded to the distributions of the plasma temperature and velocity in the vertical plane (X–Z), respectively. Inside the torch, the maximum temperature in front of the cathode is nearly 31,000 K, while the largest velocity of more than 2700 m/s is located in the channel of the anode nozzle. After entering the ambient environment, the plasma jet experiences an expansion process, and both the plasma temperature and velocity gradually decrease with the increasing of the stand-off distance.

The radial temperatures of the plasma jet at three representative injection positions are shown in Fig. 2(c). Injections 1, 2 and 3 indicate the positions of suspension injection away from the outlet of the plasma gun with distances of 8, 18 and 28 mm, respectively. At a traditional injection position (Injection 1), the profile shows the temperature of the plasma core to be 12683 K. When the injection position is changed to Injection 2, the temperature decreases to 10,999 K. A lower temperature of 7640 K is obtained when the distance between the injection position and the outlet of the plasma gun further increases to 28 mm (Injection 3).

Further, the temperature gradients of the corresponding injection positions are calculated and presented in Fig. 2(d). As seen in Fig. 2(d), there is a primary maximum value at the radial position of 2.99 mm and a second maximum at 5.28 mm for Injection 1. This implies that there is a tremendous thermophoretic force, which is calculated by the following formula (Ref 16):

$$F_T = -4\pi r_w^2 \frac{4}{15} \frac{\kappa \nabla T}{\sqrt{2\pi k_B T_0/m}} \tag{Eq 1}$$

where  $r_w$ ,  $\nabla T$ ,  $T_0$  and  $m$  correspond to the radius of a particle, the temperature gradient of the plasma flow, the surface temperature and the mass of a particle, respectively. As shown in Eq 1, the thermophoretic force is proportional to the temperature gradient.

The numerical results clarify why fragmented droplets of the suspension cannot be easily injected into the plasma core at high plasma power. For the existence of a thermophoretic force, the fragmented droplets must have a momentum to overcome the obstruction. It must be noted that the velocity of the fragmented droplets cannot be too high so as to disturb the stability of the flow field, otherwise this results in decreased deposition (Ref 17). Meanwhile, when the fragmented droplets present a large distribution in size, the thermophoretic force will cause uneven injection and produce a porous coating, since fine fragmented

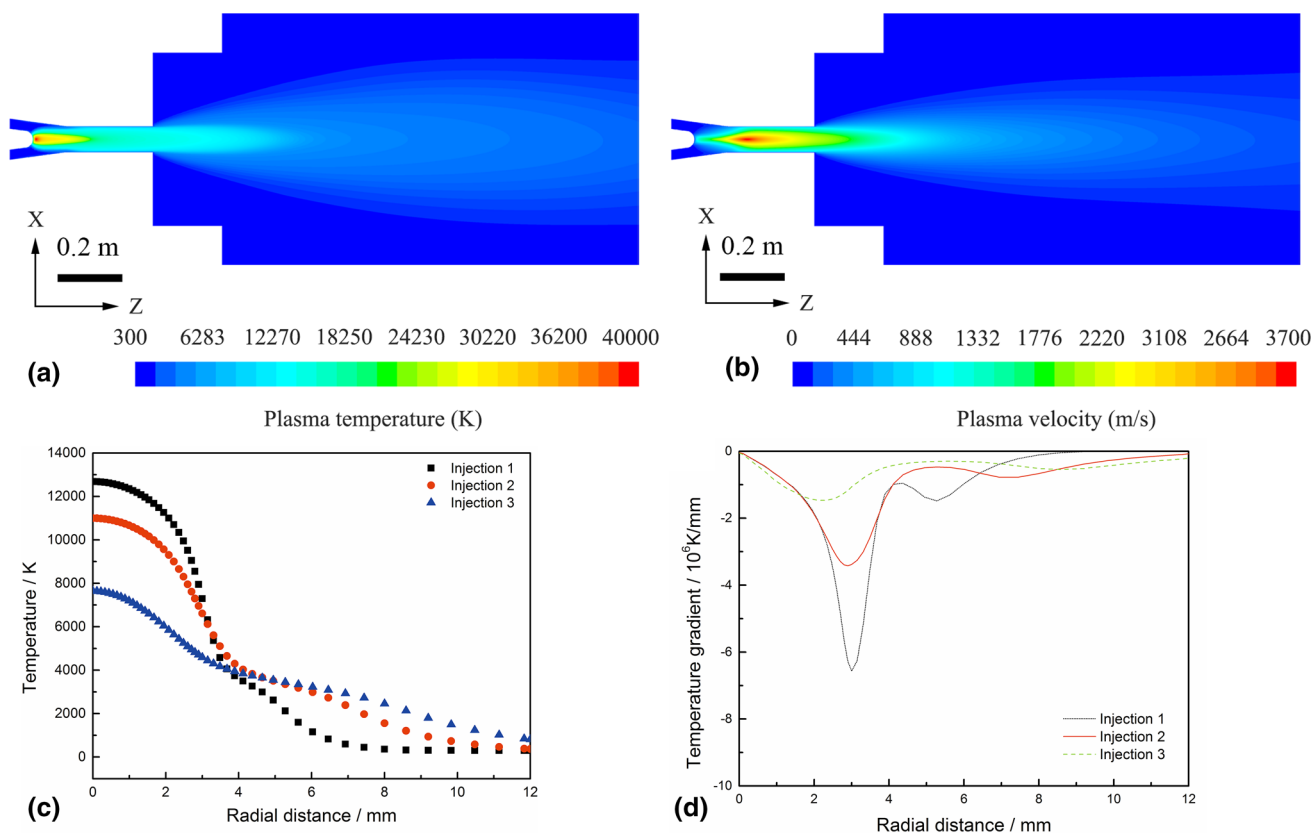


**Fig. 2** Simulation results of a more realistic 3D time-dependent LTE numerical model without suspension injection, where the computational domain included the inside and outside region of the torch (I: 650 A, P: 48.1 kW, Ar/H<sub>2</sub>: 40.0/10.0 slpm): (a) the distributions of

plasma temperature in the vertical plane, (b) the distributions of velocity in the vertical plane, (c) radial temperature profile of different injection positions, and (d) radial temperature gradient of different injection positions

droplets are prevented from taking part in coating deposition (Ref 6).

For Injection 2, the primary maximum value of the temperature gradient is decreased to half that of Injection 1, and the second maximum value is also diminished. Thus, the fragmented droplets can be easily injected into the plasma core at this position and a uniform injection can be achieved. As seen in Fig. 2(d), the temperature gradient of Injection 3 further decreases, and the profile becomes much flatter compared with Injection 2. Obviously, Injection 3 is the most favorable one for equably injecting fragmented droplets into the plasma core.

## TiO<sub>2</sub> Coating

### Coating Microstructure

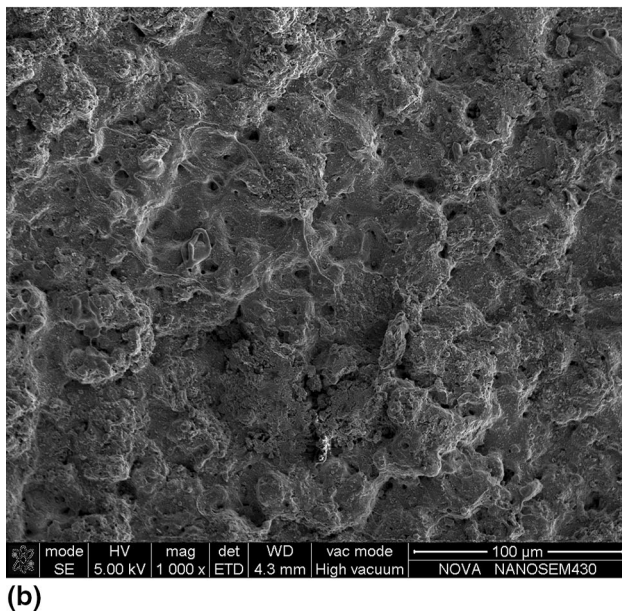
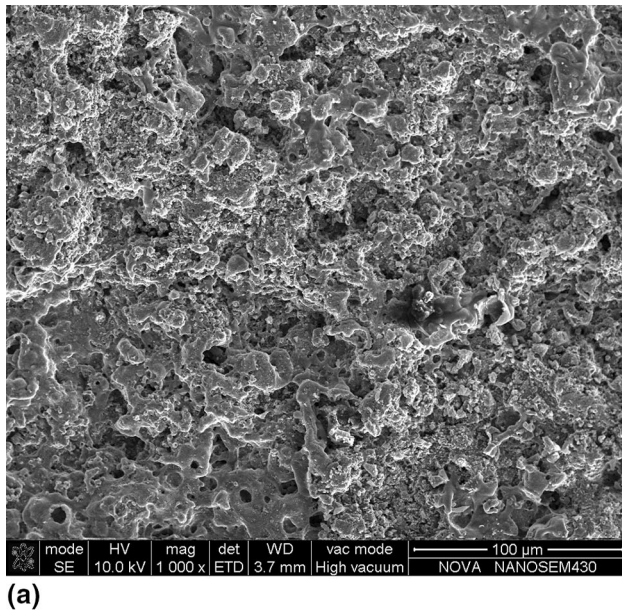
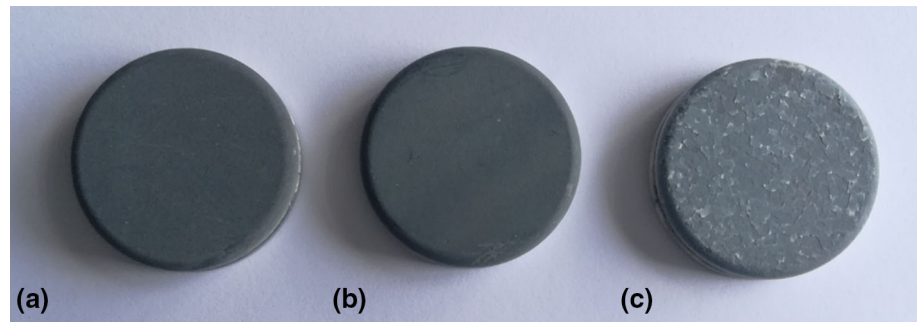
TiO<sub>2</sub> coatings of Injections 1, 2 and 3 were deposited on stainless steel substrates at a plasma power of 48.1 kW (650 A, Ar/H<sub>2</sub>: 40.0/10.0 slpm), and the corresponding samples are presented in Fig. 3. It can be seen that the as-sprayed coatings are mainly light gray-blue in color. The change from the white color of the initial TiO<sub>2</sub>

nanoparticles implies that Ti<sup>3+</sup> formed in the coatings. This can be ascribed to the high temperature reached by the plasma jet and the existence of hydrogen, causing the loss of oxygen. Interestingly, the coating deposited in Injection 3 is dappled; the areas of white spots are comprised of loose TiO<sub>2</sub> nanoparticles. After photocatalytic testing, they peel off from the coating. It seems that the short inflight time leads to insufficient interaction of TiO<sub>2</sub> particles with the plasma jet. The plasma jet vaporizes the fragmented droplets, but does not transfer enough thermal and kinetic energy to the TiO<sub>2</sub> nanoparticles to form a uniform coating. Given the dispirited deposition in Injection 3, we abandoned it for the following investigation.

The coating microstructure was further investigated by SEM. As seen in Fig. 4, both coatings are composed of undulate conglomerations and melted regions, where these conglomerations are piled up by molten and non-molten particles. The featured surface provides a large specific surface area. Thus, it can increase the reaction area between the catalyzer and degradation agent, and enhance the photocatalytic performance. In addition, many pores are observed in the TiO<sub>2</sub> coating of Injection 1.



**Fig. 3** SPS TiO<sub>2</sub> coatings with different injection positions: (a) Injection 1, (b) Injection 2 and (c) Injection 3



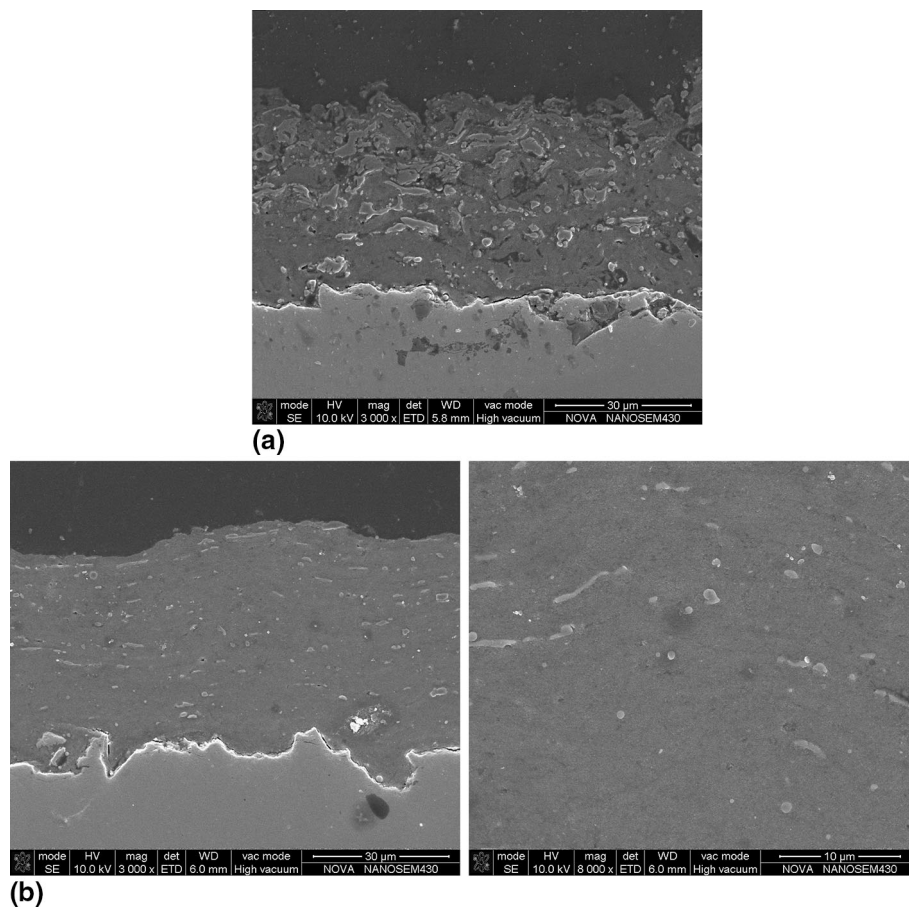
**Fig. 4** Surface SEM images of TiO<sub>2</sub> coatings: (a) Injection 1 and (b) Injection 2

Figure 5 shows the cross-section SEM images of the TiO<sub>2</sub> coatings. There are no horizontal cracks in either coating, suggesting low cooling stresses. Meanwhile, the coatings are free from vertical cracks. In comparison, the coating microstructure is strongly related to the position of the suspension injection. For Injection 1, the coating is highly porous, and consists of melted and non-melted areas. Furthermore, these melted regions are lamellar, with a length of about 20 μm. This reveals that the melted phases impinge into the substrate with high kinetic energy and make the non-melted particles stick together (Ref 8, 11). Meanwhile, the non-melted area is composed of agglomerated nanoparticles (see inset of Fig. 5(b)).

When a suspension is injected into the plasma jet, it will experience a series of complicated processes such as fragmentation, evaporation and melting. Consequently, two typical phenomena emerge, as follows (Ref 17). For these fine particles or agglomerates, they cannot be flattened as they impact the substrate with a low momentum. Thus, they pile up, with small lamellae or ultrafine lamellae. For large aggregates, they can impact the substrate with a high inertia and the lamellae melt. Based on the above analysis, the large melted regions and a large number of pores in the coating of Injection 1 reveal a nonuniform injection (Ref 6, 17). Large fragmented droplets are injected into the plasma jet, whereas fine ones are impeded from penetrating into the enthalpy source and take part in coating deposition due to thermophoretic force.

For Injection 2, the coating is relatively dense, and the cross-section presents a wave-like structure. By observation, the coating mainly consists of nanoparticles. Meanwhile, the size of the melted regions is decreased to 5 μm and they are evenly distributed throughout the coating. Thus, it shows that an efficient and uniform injection is obtained for Injection 2, which is consistent with the numerical analysis (Fig. 2d). In addition, the gravity force may also cause the structural difference of the coatings because the nanometer-sized particles lose their extremely fast velocity during suspension plasma spraying. In Injection 1, the particles have a longer flight and therefore get “lost” faster than in Injection 2, resulting in a porous

**Fig. 5** Cross-section SEM images of TiO<sub>2</sub> coatings: (a) Injection 1 and (b) Injection 2, in which the inset is a SEM image with high magnification



coating. We will evaluate the influence of the gravity force in future work.

#### Phase Compositions

X-ray diffraction was performed to assess the phase compositions of the TiO<sub>2</sub> coatings with different injection positions, and the results are illustrated in Fig. 6. The anatase content in the coatings,  $\eta$ , was calculated through the equation provided in Berger-Keller et al. (Ref 18):

$$\eta = 8I_A / [8I_A + 13I_R] \quad (\text{Eq 2})$$

where  $I_A$  and  $I_R$  are the diffraction intensities of anatase and rutile, respectively. Furthermore, crystal size,  $t$  was determined using the Scherrer formula:

$$t = K\lambda / B \cos \theta \quad (\text{Eq 3})$$

where  $K$  is the shape factor,  $\lambda$  is the wavelength of the x-ray,  $\theta$  is the Bragg angle, and  $B$  is the full width of half maximum (FWHM) of the peak intensity. All FWHMs are calibrated to the instrumental errors (Ref 19). It must be pointed out that the Scherrer formula for powders is more favorable in view of the error. Thus we tend to interpret the calculated data between coatings.

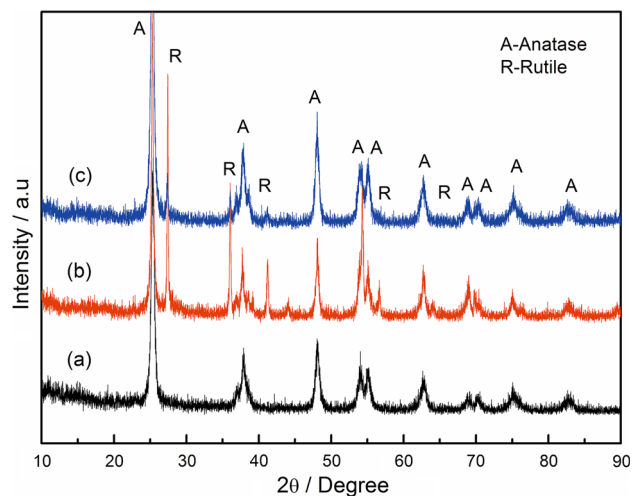


**Fig. 6** XRD patterns of TiO<sub>2</sub> coatings: (a) initial TiO<sub>2</sub> powder, (b) TiO<sub>2</sub> coating of Injection 1, and (c) TiO<sub>2</sub> coating of Injection 2

Table 1 shows the phase compositions and the crystalline sizes of the different samples. It can be clearly seen that the anatase content depends significantly on the position of the suspension injection. The initial particles containing 99.8% anatase phase has a crystalline average size

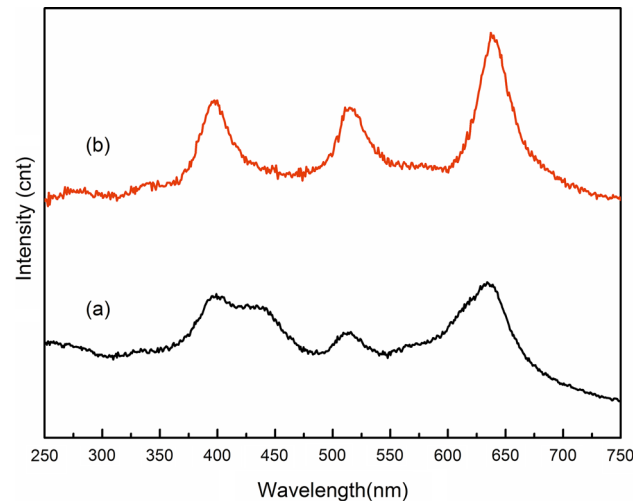
**Table 1** Phases and crystallites sizes of TiO<sub>2</sub>

Samples	Anatase, vol.%	Anatase crystallites average size, nm	Rutile crystallites average size, nm
TiO <sub>2</sub> powders	99.80	29.87	...
Injection 1	61.24	52.10	125.15
Injection 2	93.90	34.18	86.85

of 29.87 nm. For the TiO<sub>2</sub> coating deposited in Injection 1, the anatase content decreases to 61.24%, and the anatase and rutile crystallites sizes are 52.10 and 125.15 nm, respectively. In contrast, the anatase content of the TiO<sub>2</sub> coating deposited in Injection 2 is 93.9%. The crystal size of the anatase is 34.18 nm, whereas that of rutile is 86.85 nm. In brief, the XRD results coincide with the SEM analysis. The TiO<sub>2</sub> coating deposited in Injection 1 has larger molten regions consisting entirely of rutile phase, whereas the TiO<sub>2</sub> coating deposited in injection 2 presents a fine nanostructure, in which the anatase content and crystal size are comparable with those of the initial feedstock.

The diversified phase structure of the TiO<sub>2</sub> coatings can be further explained by the solidification pathway of the molten titanium, which is modified by the position of the suspension injection. After injection into the plasma jet, the solution in the droplets instantly volatilizes due to the high enthalpy of the plasma jet. Then, agglomerates begin to melt with the heating of the plasma jet, and resolidify to rutile or anatase depending on the crystallization conditions. With a high quenching rate, the molten mass can nucleate into anatase at a temperature lower than 2057 K due to the lower surface energy compared to rutile ( $\gamma_{\text{Anatase}} = 0.38 \text{ J m}^{-2}$ ,  $\gamma_{\text{Rutile}} = 0.93 \text{ J m}^{-2}$ ) (Ref 10). When the temperature is close to the melting point of TiO<sub>2</sub>, it will solidify stably into rutile (Ref 12, 20). The research work of Bannier et al. (Ref 11) verified that inflight particles in SPS deposition with a moderate arc current (400 A) displayed a higher anatase content than the coatings, and most of the phase transformation from anatase to rutile occurred after the particles imposition onto the substrate.

The agglomerates in Injection 2 experienced lower heating in comparison to Injection 1, and underwent a homogeneous nucleation and recrystallized to metastable anatase. Thus, a nanostructured TiO<sub>2</sub> coating with anatase content 93.9% and crystallites size 34.18 nm was obtained. For Injection 1, most of the TiO<sub>2</sub> agglomerates subjected to the plasma experienced a higher temperature. They solidified to form a stable rutile with the drive of Gibbs free energy and the anatase content was decreased to 61.24%. As there was longer flight distance for the growth, the rutile crystallites was increased to

**Fig. 7** Raman spectra of TiO<sub>2</sub> coatings: (a) Injection 1 and (b) Injection 2

86.85 nm, and the crystallites size of the anatase was augmented to 34.18 nm.

In addition, cooling the substrate can address the solidification pathway of TiO<sub>2</sub> agglomerates and generate metastable anatase phase. However, it is harmful to the coating microstructure, and usually results in depressed binding force and micro-defects, such as cracks (Ref 11).

#### Raman Spectra

Raman spectroscopy was also performed to characterize the phase compositions of the TiO<sub>2</sub> coatings (Fig. 7). It is used with the XRD technique because the laser focuses on the sample surface without penetrating into the coating. Thus, Raman spectroscopy can provide an insight into phase compositions on the coating surface.

For the coating of Injection 2, a typical spectrum was obtained. There are sharp peaks at 399, 513 and 639 cm<sup>-1</sup>, which are identified as B<sub>1g</sub>, A<sub>1g</sub> and E<sub>g</sub>, respectively (Ref 8). These peaks evidently indicate that the coating is composed entirely of anatase phase. Moreover, for the coating of Injection 1, two peaks at about 400 and 640 cm<sup>-1</sup> become wide. Since the characteristic peaks of E<sub>g</sub> and A<sub>1g</sub> in rutile phase are located at approximately 447 and 612 cm<sup>-1</sup>, respectively, the broadening of these two



peaks indicate the existence of the rutile phase. XRD analysis shows that the TiO<sub>2</sub> coating for Injection 2 has an anatase content of 93.9%, whereas for Injection 1 it is 61.24%. The results of Raman spectra coincide with the XRD data.

#### UV-Vis Reflectance Spectra

UV-Vis diffuse reflectance spectra were recorded with the wavelength in the range of 250–700 nm. Figure 8 shows the corresponding spectra of the initial powder and the TiO<sub>2</sub> coatings. For the starting TiO<sub>2</sub> powder with more than 99% anatase, the absorbance begins with the wavelength lower than 400 nm, which is derived from the charge transfer from the valence band to the conduction band (Ref 21). The former is generated by the 2*p* orbitals of oxide anions, whereas the latter is caused by the 3*d t<sub>2g</sub>* of Ti<sup>4+</sup>. For the TiO<sub>2</sub> coatings, both have an absorbance edge in the range of 390–410 nm which is correlated with a typical band gap of 3.0–3.2 eV.

By observation, the TiO<sub>2</sub> coatings display a broad absorbance compared with the initial powder. Meanwhile, the maximum reflectance shifts to a higher wavelength. This could be explained by the presence of a mixture of anatase and rutile phases in the coatings. The energy band of the rutile is 3.0 eV (420 nm), whereas the energy band of the anatase changes to 3.2 eV (390 nm). Thus, the TiO<sub>2</sub> coatings show a wide absorbance range. Moreover, the rutile content for Injection 1 is higher than that of Injection 2. As a result, the absorbance range of the former is obviously prolonged to a higher wavelength.

In addition, the TiO<sub>2</sub> coatings demonstrate visible light absorbance. When the wavelength is longer than 450 nm, the reflectance distinctly decreases with the increased wavelengths. The spectra data coincide with the

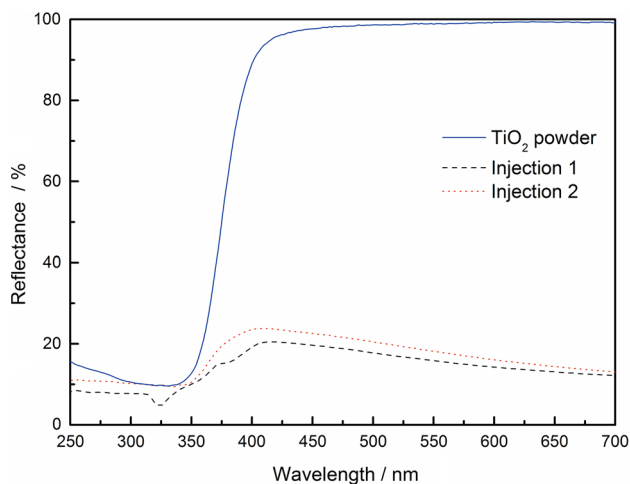


**Fig. 8** UV-Vis diffuse reflectance of raw TiO<sub>2</sub> powder and TiO<sub>2</sub> coatings

experimental phenomenon. As shown in Fig. 3, these samples are light gray-blue in color. Robinson et al. (Ref 10) ascribed the absorbance to the appearance of Ti<sup>3+</sup> in the TiO<sub>2</sub> coatings due to the loss of oxygen.

#### Photocatalytic Activity

All samples were immersed in MB solution with UV irradiation, and then the MB concentrations were measured at regular intervals, and the corresponding results are displayed in Fig. 9.

As seen in Fig. 9, the blank substrate exhibits little change to the MB concentration within 12 h except for a slight decrease in the first 1.5 h. For both the coated samples, the rapid declines of MB concentrations with irradiation time are evident, which verifies the photocatalytic activities of the TiO<sub>2</sub> coatings. In comparison, the TiO<sub>2</sub> coating deposited in Injection 2 presents a higher degradation efficiency than Injection 1 after 2.5 h UV irradiation. The reason is the TiO<sub>2</sub> coating of Injection 2 has a higher anatase content and smaller crystalline size than that of Injection 1. Due to a decreased electron-hole recombination, the anatase phase is more active than the rutile. Therefore, the TiO<sub>2</sub> coating of Injection 2 exhibits an increased photoactivity during the UV irradiation. In addition, the degradation efficiency of the TiO<sub>2</sub> coating deposited in Injection 1 is comparable to that deposited in Injection 2 within 2.5 h UV irradiation, though the latter has a higher anatase content and smaller crystalline size than the former. The reason is that the TiO<sub>2</sub> coating of Injection 1 has many pores (Fig. 4a). The values of surface roughness are 4.95 and 4.37 μm for the TiO<sub>2</sub> coating of Injection 1 and Injection 2, respectively. Those pores increase the reaction area between the catalyzer and the

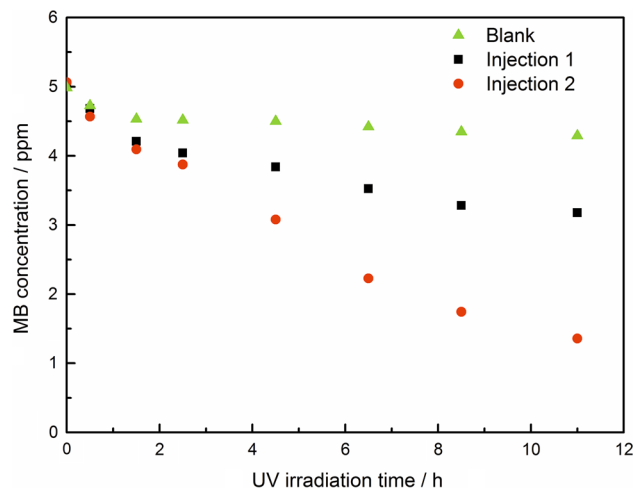


**Fig. 9** Variation of MB concentrations with UV irradiation time of the TiO<sub>2</sub> coatings and a blank sample



degradation agent, and enhance the photocatalytic performance at the initial stage of UV irradiation.

In all, the results are comparable with the research work of Bannier et al. (Ref 11). They reported that the photocatalytic activity of SPS TiO<sub>2</sub> coatings fitted well to a first-order kinetic model, and the values of the kinetic constant for these coatings were higher than a commercial sol–gel coating.

Interestingly, there are many literature reports of the photocatalytic performance of TiO<sub>2</sub> coatings which were not linearly correlated with the anatase phase content. Two reasons could be as follows: first, the phase composition measured using XRD is distinguished by the nature of coating surface. Quantitative analysis based on Raman spectra is needed to characterize the phase composition on the coating surface because it penetrates a few micrometers. Second is that the status of the coating surface complicates the photocatalytic process. The hydroxylation (Ref 22, 23), defects, and adsorption behavior must be considered. Thus, further work will be focused on the surface properties of the TiO<sub>2</sub> coating for Injection 2 to clarify the photocatalytic behavior, and subsequently maximize its photocatalytic activity.

## Conclusion

With the guidance of numerical simulation derived from a realistic 3D time-dependent numerical model that included the inside and outside of torch regions, TiO<sub>2</sub> coatings deposited using different injection positions were reviewed.

For the traditional position (Injection 1), the temperature of the plasma core reached 12,683 K, which presented a maximum value of temperature gradient at the radial position of 2.99 mm. The temperature gradient initiated a tremendous thermophoretic force to impede fragmented droplets from penetrating the plasma core unequally, resulting in a porous TiO<sub>2</sub> coating.

Adopting the modified position (Injection 2), the thermophoretic force was decreased to half of that of Injection 1. Then, fragmented droplets were uniformly injected into the plasma core, and an adhesive TiO<sub>2</sub> coating was deposited onto stainless steel. Meanwhile, as the plasma temperature was decreased in comparison to Injection 1, it modified the solidification pathway of the melted TiO<sub>2</sub> particles and made them nucleate into anatase. Consequently, a nanostructured TiO<sub>2</sub> coating with anatase content of 93.9% was obtained at the plasma power of 48.1 kW, which showed the desired photocatalytic activity to degrade an aqueous solution of methylene blue.

In all, the study provided a novel idea to limit the heat and modify the solidification pathway of melted TiO<sub>2</sub> particles without decreasing the plasma power.

**Acknowledgment** This work has been financially supported by Guangdong Natural Science Foundation (2016A030312015), Guangdong Academy of Sciences (2017GDASCX-0843, 2016GDASPT-0206, 2016GDASPT-0317).

## References

- V.C. Sarasidis, K.V. Plakas, S.I. Patsios, and A.J. Karabelas, Investigation of Diclofenac Degradation in a Continuous Photocatalytic Membrane Reactor, *Influ. Oper. Parameters Chem. Eng. J.*, 2014, **239**, p 299-311
- Y.R. Smith, R.S. Ray, K. Carlson, B. Sarma, and M. Misra, Self-Ordered Titanium Dioxide Nanotube Arrays: Anodic Synthesis and Their Photo/Electro-Catalytic Applications, *Materials*, 2013, **6**(7), p 2892-2957
- D. Avisar, I. Horovitz, L. Lozzi, F. Ruggieri, M. Baker, M.-L. Abel, and H. Mamane, Impact of Water Quality on Removal of Carbamazepine in Natural Waters by N-doped TiO<sub>2</sub> Photocatalytic Thin Film Surfaces, *J. Hazard. Mater.*, 2013, **244**, p 463-471
- D. Chen, E.H. Jordan, and M. Gell, Porous TiO<sub>2</sub> Coating Using the Solution Precursor Plasma Spray Process, *Surf. Coat. Technol.*, 2008, **202**(24), p 6113-6119
- S. Kozerski, F.L. Toma, L. Pawlowski, B. Leupolt, L. Latka, and L.M. Berger, Suspension Plasma Sprayed TiO<sub>2</sub> Coatings Using Different Injectors and Their Photocatalytic Properties, *Surf. Coat. Technol.*, 2010, **205**(4), p 980-986
- F.L. Toma, G. Bertrand, D. Klein, C. Coddet, and C. Meunier, Nanostructured Photocatalytic Titania Coatings Formed by Suspension Plasma Spraying, *J. Therm. Spray Technol.*, 2006, **15**(4), p 587-592
- P. Swarnakar, S.R. Kanel, D. Nepal, Y. Jiang, H. Jia, L. Kerr, M.N. Goltz, J. Levy, and J. Rakovan, Silver Deposited Titanium Dioxide Thin Film for Photocatalysis of Organic Compounds Using Natural Light, *Sol. Energy*, 2013, **88**, p 242-249
- L. Du, T.W. Coyle, K. Chien, L. Pershin, T. Li, and M. Golozar, Titanium Dioxide Coating Prepared by Use of a Suspension-Solution Plasma-Spray Process, *J. Therm. Spray Technol.*, 2015, **24**(6), p 1-10
- P. Daram, C. Banjongprasert, W. Thongsuwan, and S. Jiansirisomboon, Microstructure and Photocatalytic Activities of Thermal Sprayed Titanium Dioxide/Carbon Nanotubes Composite Coatings, *Surf. Coat. Technol.*, 2016, **306**, p 290-294
- B.W. Robinson, C.J. Tighe, R.I. Gruar, A. Mills, I.P. Parkin, A.K. Tabecki, H.L. de Villiers Lovelock, and J.A. Darr, Suspension Plasma Sprayed Coatings Using Dilute Hydrothermally Produced Titania Feedstocks for Photocatalytic Applications, *J. Mater. Chem. A*, 2015, **3**(24), p 12680-12689
- E. Bannier, G. Darut, E. Sánchez, A. Denoirjean, M.C. Bordes, M.D. Salvador, E. Rayón, and H. Ageorges, Microstructure and Photocatalytic Activity of Suspension Plasma Sprayed TiO<sub>2</sub> Coatings on Steel and Glass Substrates, *Surf. Coat. Technol.*, 2011, **206**(2-3), p 378-386
- G. Mauer, A. Guignard, and R. Vaßen, Plasma Spraying of Efficient Photoactive TiO<sub>2</sub> Coatings, *Surf. Coat. Technol.*, 2013, **220**(5), p 40-43
- Z. Guo, S. Yin, H. Liao, and S. Gu, Three-Dimensional Simulation of an Argon-Hydrogen DC Non-transferred Arc Plasma Torch, *Int. J. Heat Mass Transf.*, 2015, **80**, p 644-652

14. M. Alaya, C. Chazelas, and A. Vardelle, Parametric Study of Plasma Torch Operation Using a MHD Model Coupling the Arc and Electrodes, *J. Therm. Spray Technol.*, 2015, **25**(1), p 1-8
15. R. Bolot, C. Coddet, A. Allimant, and D. Billières, Modeling of the Plasma Flow and Anode Region Inside a Direct Current Plasma Gun, *J. Therm. Spray Technol.*, 2011, **20**(1-2), p 21-27
16. E. Pfender and Y.C. Lee, Particle Dynamics and Particle Heat and Mass Transfer in Thermal Plasmas. Part I. The Motion of a Single Particle Without Thermal Effects, *Plasma Chem. Plasma Process.*, 1985, **5**(3), p 211-237
17. W. Fan and Y. Bai, Review of Suspension and Solution Precursor Plasma Sprayed Thermal Barrier Coatings, *Ceram. Int.*, 2016, **42**(13), p 14299-14312
18. N. Berger-Keller, G. Bertrand, C. Filiatre, C. Meunier, and C. Coddet, Microstructure of Plasma-Sprayed Titania Coatings Deposited from Spray-Dried Powder, *Surf. Coat. Technol.*, 2003, **168**(2-3), p 281-290
19. Z. Pala, E. Shaw, J.W. Murray, N. Senin, and T. Hussain, Suspension High Velocity Oxy-Fuel Spraying of TiO<sub>2</sub>: A Quantitative Approach to Phase Composition, *J. Eur. Ceram. Soc.*, 2017, **37**(2), p 801-810
20. D.A.H. Hanaor and C.C. Sorrell, Review of the Anatase to Rutile Phase Transformation, *J. Mater. Sci.*, 2011, **46**(4), p 855-874
21. J.O. Carneiro, S. Azevedo, F. Fernandes, E. Freitas, M. Pereira, C.J. Tavares, S. Lancers-Méndez, and V. Teixeira, Synthesis of Iron-Doped TiO<sub>2</sub> Nanoparticles by Ball-Milling Process: The Influence of Process Parameters on the Structural, Optical, Magnetic, and Photocatalytic Properties, *J. Mater. Sci.*, 2014, **49**(21), p 7476-7488
22. F.-L. Toma, G. Bertrand, S. Begin, C. Meunier, O. Barres, D. Klein, and C. Coddet, Microstructure and Environmental Functionalities of TiO<sub>2</sub>-Supported Photocatalysts Obtained by Suspension Plasma Spraying, *Appl. Catal. B*, 2006, **68**(1), p 74-84
23. P. Ctibor, Z. Pala, J. Sedláček, V. Štengl, I. Píš, T. Zahoranová, and V. Nehasil, Titanium Dioxide Coatings Sprayed by a Water-Stabilized Plasma Gun (WSP) with Argon and Nitrogen as the Powder Feeding Gas: Differences in Structural, Mechanical and Photocatalytic Behavior, *J. Therm. Spray Technol.*, 2012, **21**(3-4), p 425-434